Electron transport probing the electrically tunable topological phase transition in a Dirac semimetal

Shunxi Tang,[1] Wang Chen [●],[2] Qian Ye,[1] Zhengfang Liu,[3] Qingping Wu,[3] Yan Du,[1] Xiaoying Zhou [●],[2] and Xianbo Xiao [●][1,*]

[1]*School of Computer Science, Jiangxi University of Chinese Medicine, Nanchang 330004, China*
[2]*Department of Physics, Key Laboratory for Low-Dimensional Structures and Quantum Manipulation (Ministry of Education), Hunan Normal University, Changsha 410081, China*
[3]*Department of Applied Physics, East China Jiaotong University, Nanchang 330013, China*

Electron transport in a Dirac semimetal (DSM) quantum wire without/with an external electric field is investigated by using the Green-function-based Landauer-Büttiker formula. Normal-topological phase transition is certificated by the different characteristics between the DSM quantum wire without and with the electric field, including the orbital decomposition for the energy bands, transversally local charge and spin polarization density distributions, topological Chern number, transport behaviors, and disorder effects. Topologically trivial surface states are found in the former system and their transport can be localized by disorders. However, topologically nontrivial surface states are generated in the latter one and their transport is robust against strong disorders when the electric field strength is larger than a critical value. In addition, switching effect of the electron transport in the DSM quantum wire can be achieved by varying the electric field strength. Further studies indicate that the switching effect shows a strong robustness against disorder, displaying the feasibility of designing a topological field effect transistor based on the considered system.

I. INTRODUCTION

Topological materials, which own nontrivial topologies encoded in their electronic energy bands and wave functions, have drawn enormous attention in the past decade [1–3]. They can be classified further into topological insulators (TIs) [4,5] or Dirac semimetals (DSMs) [6–8] by considering if there are gaps in their energy bands or not. Therefore, the topological characteristic revolutionized the traditional classification of materials. Another important feature of topological materials is that Dirac-electron-like and Fermi arc states can be found at the boundaries once the TIs and DSMs are confined, respectively [9–11]. These states are spin-momentum locking and protected by the time reversal symmetry, resulting in the fact that the backscattering induced by nonmagnetic disorders is forbidden. Consequently, topological materials may find implications in designing electron or spin devices with ultralow power dissipation.

Manipulating the boundary states transport in topological materials by electrical means is one of the most key prerequisites during their applications in topological electronic devices. Both the spin and charge transport of the edge states in electrically constricted TI quantum point contacts can be switched on or off thanks to the coupling between the opposite edge states [12–14]. Spin rotation and analysis are predicted in a local top-gate modulated TI quantum wire since the gate voltage brings an external phase to one of the two edge states [15]. Quantized tunneling probabilities between 0 and 1 can be achieved in a transversal electric field modulated TI nanoribbon, which may provide a new strategy for the design

of topological transistors [16]. Meanwhile, a perpendicular electric field modifies the Fermi velocity and dispersion relation of the surface states in topological semimetal thin film, which will, in turn, affect the transport properties [17]. Furthermore, the positions of the surface energy subbands of DSM nanowires can be shifted by the static electric potential of the lateral gates, leading to the gate-voltage-controlled surface states transport [18,19].

On the other hand, topological phase transition (TPT) in topological materials is another important issue in the design-ment of topological electronic devices because of the different transport properties in different phases. Oscillating topologically trivial and nontrivial phases are found in both TI [20,21], DSM [8,22,23], and Weyl semimetal [24] thin films when varying the thickness of the thin film. Moreover, normal-topological phase transition can also be driven by an electric field in these systems. It is found that the intrinsic built-in electric field in GaN/InN/GaN [25] and GaAs/Ge/GaAs [26] quantum well will reduce their band gaps and enhance the spin-orbit coupling strength, leading to a normal-topological insulator transition. Recently, a similar TPT is also predicted theoretically in a DSM thin film by applying a perpendicular electric field [27,28]. Later, the angle-resolved photoelectron spectroscopy and scanning tunneling spectroscopy measure-ments have verified this prediction. The experimental results indicate that a TI phase with bulk band gaps greater than 300.0 meV and a conventional insulator phase with a band gap of 90.0 meV can be achieved in the monolayer Na_3Bi by tuning the perpendicular electric field strength [29]. There-fore, the monolayer Na_3Bi may be suitable for the designment of a room-temperature topological transistor. However, the electron transport measurement, which is an intuitive method for the verification of the TPT and important for practical applications as well, has not been performed in the DSM up to

---

*Author to whom correspondence should be addressed: 20101034@jxutcm.edu.cn
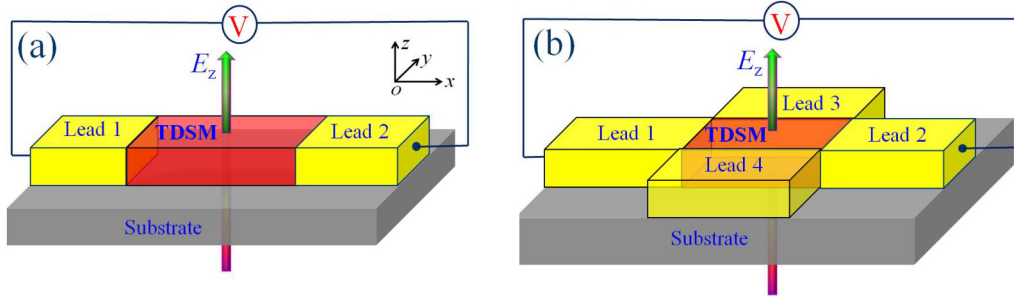
205427-1

FIG. 1. Schematic figure showing the two- (a) and four-terminal (b) DSM quantum wire with an external electric field along the *z*-axis direction.

date. Therefore, a natural question is raised if the TPT can be verified by the transport measurement since it can be carried out easily in DSM quantum wires.

In this paper we investigate the orbitally resolved energy bands, transversally local charge and spin polarization density distributions, topological Chern number, transport behaviors, and disorder effects of the DSM quantum wires without/with an external electric field. The obtained results indicate that electric-field-induced TPT happens in the DSM. Moreover, alternative switch on and off states of the electron transport in the two-terminal DSM quantum wires can be obtained by varying the electric field strength. Further studies also show that the electron transport is robust against disorders. Therefore, we propose an all-electric topological field effect transistor based on the considered system.

The rest of this paper is arranged as follows. In Sec. II, theoretical model of the considered system and calculation methods are presented. In Sec. III, numerical results and discussions are demonstrated. Finally, Sec. IV concludes the paper.

II. MODEL AND METHODS

Figures 1(a) and 1(b) schematically show the two- and four-terminal DSM quantum wires subject to an electric field along the *z*-axis direction, respectively. The results obtained in this paper do not depend on the particular DSM material. Here, for concreteness, we take Na$_3$Bi as an example, which has been experimentally demonstrated as a three-dimensional (3D) DSM material [30]. Its low-energy physics is described by the four-band model around the Γ point of the Brillouin zone. Written in the basis of $|S_{\frac{1}{2}}^+, \frac{1}{2}\rangle$, $|P_{\frac{3}{2}}^-, \frac{3}{2}\rangle$, $|S_{\frac{1}{2}}^+, -\frac{1}{2}\rangle$, and $|P_{\frac{3}{2}}^-, -\frac{3}{2}\rangle$, where S and P denote, respectively, the electron and hole subbands, the 4×4 Hamiltonian takes the form [7]

$$H(\mathbf{k}) = h_0(\mathbf{k}) + \begin{pmatrix} h_\mathbf{k}^\uparrow & 0 \\ 0 & h_\mathbf{k}^\downarrow \end{pmatrix}, \quad (1)$$

in which

$$h_\mathbf{k}^\uparrow = \begin{pmatrix} M(\mathbf{k}) & Ak_+ \\ Ak_- & -M(\mathbf{k}) \end{pmatrix} = M(\mathbf{k})\sigma_z + A(k_x\sigma_x - k_y\sigma_y),$$

$$h_\mathbf{k}^\downarrow = \begin{pmatrix} M(\mathbf{k}) & -Ak_- \\ -Ak_+ & -M(\mathbf{k}) \end{pmatrix} = M(\mathbf{k})\sigma_z - A(k_x\sigma_x + k_y\sigma_y),$$

and $h_0(\mathbf{k}) = C_0 + C_1 k_z^2 + C_2(k_x^2 + k_y^2)$, $M(\mathbf{k}) = M_0 - M_1 k_z^2 - M_2(k_x^2 + k_y^2)$, $k_\pm = k_x \pm ik_y$, $\mathbf{k} = (k_x, k_y, k_z)$ is the wave vector, σ_i ($i = x, y, z$) is the ordinary Pauli matrix, and $\uparrow / \downarrow$ denotes the spin up/down state.

Solving the secular equation of the Hamiltonian in Eq. (1), we find the energy band of the DSM is $E_\pm = h_0 \pm h$, where $+ (-)$ denotes the conduction (valence) band, $h = \sqrt{h_x^2 + h_y^2 + h_z^2}$ with $h_x = Ak_x s_z$, $h_y = Ak_y$, and $h_z = M(\mathbf{k})$, $s_z = \pm 1$ indicates the spin up/down. The corresponding wave functions are

$$\psi_{\pm,\mathbf{k}} = \frac{e^{i\mathbf{k}\cdot\mathbf{r}}}{\sqrt{2h(h \mp h_z)}} \begin{pmatrix} h_x + ih_y \\ \pm h - h_z \end{pmatrix}, \quad (2)$$

where $\psi_{+,\mathbf{k}}$ ($\psi_{-,\mathbf{k}}$) is the wave function of the conduction (valence) band.

As the transport properties of the considered system in the present work are mainly determined by the confinement and electric field effects along *z*-axis direction, we only calculate the *z* component of Berry curvature

$$\Omega_n(\mathbf{k}) = i \sum_{n' \neq n} \frac{\langle \psi_{n\mathbf{k}} | \frac{\partial H}{\partial p_x} | \psi_{n'\mathbf{k}} \rangle \langle \psi_{n'\mathbf{k}} | \frac{\partial H}{\partial p_y} | \psi_{n\mathbf{k}} \rangle - (x \leftrightarrow y)}{(E_n - E_{n'})^2}. \quad (3)$$

After some tedious deductions, the spin-resolved Berry curvature in the conduction band is obtained as

$$\Omega_c^{s_z}(\mathbf{k}) = s_z \frac{A^2(B + M_2 k_s^2)}{2[A^2 k_s^2 + (B - M_2 k_s^2)^2]^{3/2}} = \Omega_c^{s_z}(-\mathbf{k}), \quad (4)$$

where $k_s = \sqrt{k_x^2 + k_y^2}$ and $B = M_0 - M_1 k_z^2$. According to the equation of Berry curvature, in the valence band, we have $\Omega_v^{s_z}(\mathbf{k}) = -\Omega_c^{s_z}(\mathbf{k})$. At the same time, for the opposite spin, we have $\Omega^{-s_z}(\mathbf{k}) = -\Omega^{s_z}(\mathbf{k})$. Consequently, the spin-resolved topological Chern number for the conduction band is given by

$$C^{s_z} = \frac{s_z}{2} \int_0^\infty \frac{A^2(B + M_2 k_s^2)}{2[A^2 k_s^2 + (B - M_2 k_s^2)^2]^{3/2}} dk_s^2. \quad (5)$$

By defining $F = \frac{B - M_2 k_s^2}{\sqrt{A^2 k_s^2 + (B - M_2 k_s^2)^2}}$, we have $\frac{\partial F}{\partial k_s^2} = -\frac{\Omega^{s_z}}{s_z}$ so that the spin-resolved topological Chern number of each conduction band is

$$C^{s_z} = -\frac{s_z}{2} F|_0^\infty = \frac{s_z}{2}[\text{sgn}(M_2) + \text{sgn}(M_0 - M_1 k_z^2)]. \quad (6)$$
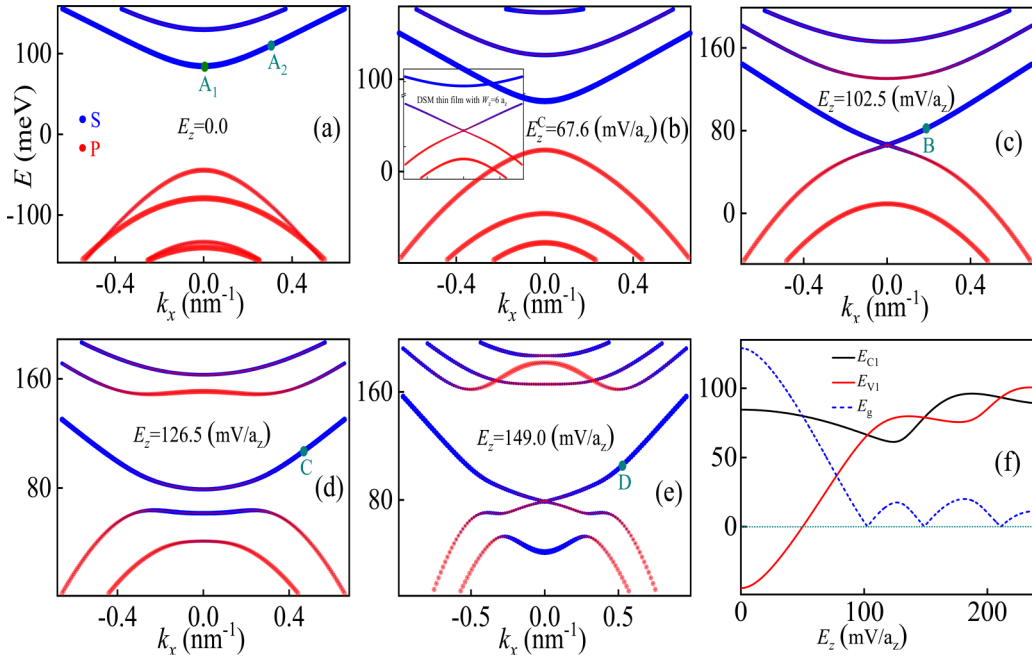
FIG. 2. Orbital decompositions for the energy band of the infinitely long DSM quantum wire along the x-axis direction with different electric field strengths $E_z = 0.0$ (a), 67.6 (b), 102.5 (c), 126.5 (d), and 149.0 mV/a_z (e). Thicker lines indicate a more dominant contribution. The transversal widths of the quantum wire are taken as $W_y = 20a_y$ and $W_z = 6a_z$. Inset in (b) showing the orbital decompositions for the energy band of a DSM thin film with the thickness $W_z = 6a_z$. (f) The energy band gap (blue dashed line), lowest conduction (black solid line), and highest valence (red solid line) subbands of the DSM quantum wire at $k_x = 0.0$ as a function of the electric field strength.

The transport properties of the two- and four-terminal DSM quantum wires are studied using the Landauer-Büttiker formalism combined with nonequilibrium Green's function method. The total transmission probability of all the propagating modes between any two leads is given by [31]

$$T_{\beta\alpha} = \text{Tr}[\Gamma_\beta G^r \Gamma_\alpha G^a], \qquad (7)$$

where $G^{r/a}$ is the retarded/advanced Green's function of the whole two- or four-terminal DSM quantum wire, $\Gamma_{\alpha/\beta}$ is the linewidth function describing the coupling between the lead and DSM quantum wire, and the trace takes over both the spatial and spin degrees of freedom. The linewidth functions can be obtained from $\Gamma_\alpha = i(\Sigma_\alpha^r - \Sigma_\alpha^a)$, where $\Sigma_\alpha^{r/a}$ is the retarded/advanced self-energy for the lead α ($\alpha = 1, 2, 3,$ or 4). In the modeling we assume that all the leads are semi-infinite and have the same widths as the contacted surfaces of the DSM quantum wires. The self-energies of the leads $\Sigma_\alpha^{r/a}$ as well as the Green's function $G^{r/a}$ can be computed by using a recursive method [32].

III. NUMERICAL RESULTS AND DISCUSSIONS

According to the finite-difference method, we model the DSM quantum wires in Fig. 1 by discretizing Eq. (1) onto a 3D cubic lattice with the lattice constants $a_x = a_y = 0.5448$ nm, and $a_z = 0.4828$ nm [27]. The parameters in Eq. (1) are obtained by fitting the *ab initio* calculation results, namely $C_0 = -63.82$ meV, $C_1 = 87.536$ meV nm^2, $C_2 = -84.008$ meV nm^2, $M_0 = -86.86$ meV, $M_1 = -106.424$ meV nm^2, $M_2 = -103.610$ meV nm^2, and $A = 245.98$ meV nm [7]. In the following numerical calculations, the transversal widths of the DSM quantum

wires in Fig. 1 are $W_y = 20a_y$ and $W_z = 6a_z$. The length of the DSM quantum wire is $L_x = 50a_x$ in Fig. 1(a) and $20a_x$ in Fig. 1(b). In general, the leads can be any metals since the essential physics that we discuss below is independent of the particular leads. However, in order to minimize the contact resistance, we model the leads by using the same $H(\mathbf{k})$ in Eq. (1). The effects of the electric field can be introduced by adding an external term $eE_z z$ to the on-site energy of the lattices, where $-e$ and E_z are the electron charge and electric field strength, respectively. In addition, for the DSM quantum wire, the spin-orbit interaction term $B_1 k_z$, where B_1 is estimated to be 6.22 meV nm, should be included in the original Hamiltonian Eq. (1) since its threefold rotational symmetry is broken [7]. However, we found that this term does not change the intrinsic results obtained in this work so that it is neglected for simplicity.

A. Energy bands and electronic states of the DSM quantum wire

According to the discretized Hamiltonian of Eq. (1), the energy band $E(k_x)$, the orbital- and spin-resolved transversal wave function $\phi_{m,n,k_x}^{o,s_z}(y,z)$ of the DSM quantum wire can be obtained numerically. Here m and n are the subband indices along the y and z axis, o and s_z denote the orbital (S and P) and spin ($\uparrow$ and $\downarrow$) degrees, respectively. Figures 2(a)–2(e) show the orbital decomposition $\sum_{s_z,y,z} |\phi_{m,n,k_x}^{o,s_z}(y,z)|^2$ for the energy bands of the infinitely long (along the x axis) DSM quantum wires with different electric field strengths $E_z = 0.0, 67.6, 102.5, 126.5,$ and 149.0 mV/a_z, respectively. The blue lines represent the contribution from S orbital and the red lines stand for that from P orbital. The thickness of lines is proportional to normalized orbital contribution. Due to the finite size effect, energy band gap $E_g \approx 128.0$ meV is opened
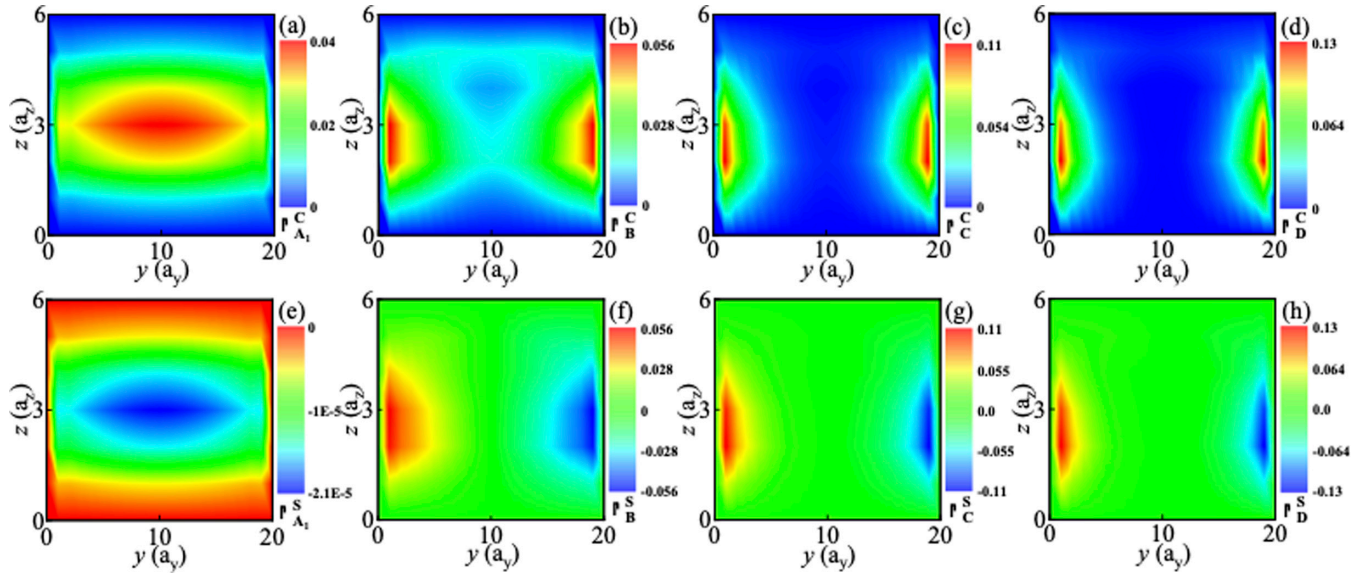
FIG. 3. (a)–(d) The transversally local charge density distributions of the DSM quantum wire for the four points A_1, B, C, and D indicated in Figs. 2(a) and 2(c)–2(e), respectively. (e)–(h) The corresponding local spin polarization density distributions with respect to (a)–(d), respectively.

at the original Dirac point $k_x = 0.0$, as shown in Fig. 2(a). Moreover, the first pair of the discretized z-axis wave vector $k_{zn} = \pm n\pi/W_z$ are $k_{z1} = \pm 1.08$ nm^{-1}, which locate outside the two Dirac point $k_z^D = \pm\sqrt{\frac{M_0}{M_1}} = \pm 0.90$ nm^{-1}. Therefore, no subband is inverted so that the DSM quantum wire is a normal band insulator. Meanwhile, the orbital contributions to the energy band display a normal order, i.e., the conduction and valence bands are contributed by the S and P orbits, respectively. As an electric field along the z-axis direction is applied to the DSM quantum wire, it couples with the subbands, which leads to the fact that the conduction subbands are lowered while the valence subbands are lifted first [27]. As a result, the band gap of the DSM quantum wire decreases as the increasing electric field strength, as shown in Fig. 2(b). Here the electric field is taken as $E_z = 67.6$ mV/a_z, which corresponds to the critical value of the TPT of the DSM thin film with the same thickness $W_z = 6a_z$. In this case, the band gap of the DSM thin film is closed, as displayed by the inset in Fig. 2(b). However, for the DSM quantum wire, the confinement is also applied along the y-axis direction, which enlarges the band gap. Therefore, a band gap with the value $E_g \approx 53.0$ meV is still observed. Furthermore, the orbital contributions to the energy band also display the normal order. However, the band gap will be closed when the electric field strength is increased to $E_z = 102.5$ mV/a_z, as shown in Fig. 2(c). As this electric field strength is larger than the critical value of the TPT, the DSM quantum wire is transformed into a TI. Consequently, parts of orbital contribution order are inverted, as shown by the bottom of the second conduction subband and the top of the first valence subband. However, differing from that of the DSM thin film, the band gap of the DSM quantum wire will be reopened, and then closed again as the electric field strength is increased further, as shown in Figs. 2(d) and 2(e), respectively. Here the electric field strengths are $E_z = 126.5$ in Fig. 2(d) and 149.0 mV/a_z

in Fig. 2(e). In addition, more parts of the orbital contribution order are inverted. However, it is noteworthy that the lowest conduction subband of the DSM quantum wire is contributed from the S orbit for all the different electric field strengths. For the sake of showing the effects of the electric field on the energy band more clearly, Fig. 2(f) displays the band gap (blue dashed line), the first conduction (black solid line) and valence subbands (red solid line) at $k_x = 0.0$ of the DSM quantum wire as a function of the electric field strength. We can see that the band gap shows an oscillating behavior with increasing electric field strength, which is consistent with evolution of the energy bands in Figs. 2(a)–2(e). The oscillating changes of the band gap upon application of the electric field are different from those of the DSM thin film, where only bulk subbands are generated in the energy band. However, for the DSM quantum wire, the surface subbands due to the confinement along the y axis also emerge in the energy band besides the bulk subbands caused by the confinement along the z axis. For example, the first conduction subband in Figs. 2(a)– 2(e), which is verified by the transversally local charge and spin density distributions of the DSM quantum wire shown in Fig. 4. Therefore, the alternative band gap closure and reopening are the behaviors of the whole energy band gap but not the bulk band gap.

The transversally local charge density distributions $\rho^C = \sum_{o,s_z} |\phi_{m,n,k_x}^{o,s_z}(y,z)|^2$ of the infinitely long DSM quantum wires (along the x axis) with different electric field strengths are demonstrated in Figs. 3(a)–3(d), which correspond to the four electron states A_1 ($E = 76.3$ meV), B ($E = 80.0$ meV), C ($E = 106.0$ meV), and D ($E = 105.0$ meV) indicated in Figs. 2(a) and 2(c)–2(e), respectively. For the DSM quantum wire without electric field, as shown in Fig. 3(a), the transversally local charge density distribution is mainly localized inside the bulk of the DSM quantum wire. However, the local charge density inside the bulk will be depleted gradually and moved toward the surfaces when the electric field is applied
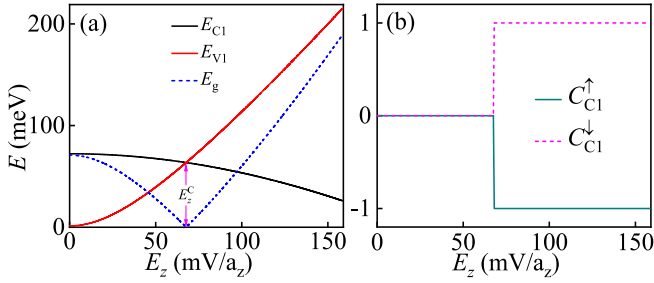
FIG. 4. (a) The first conduction (black solid line) and valence (red solid line) subbands and band gap (blue dashed line) of the DSM thin film at $k_s = 0$ as a function of the perpendicular electric field strength. The thin film thickness $W_z = 6a_z$ is the same as that of the DSM quantum wire along the z-axis direction. (b) The spin-resolved topological Chern number of the first conduction subband of the DSM thin film as a function of the electric field strength.
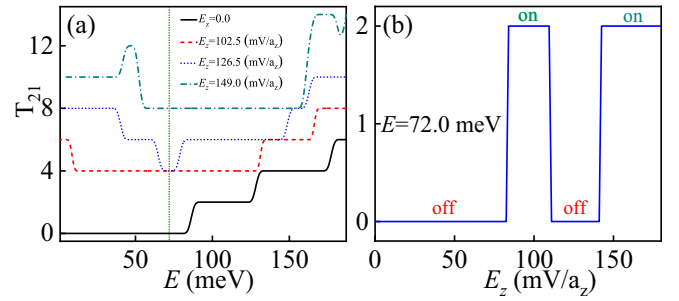

FIG. 5. (a) The transmission probability spectra of the two-terminal DSM quantum wire with different electric field strengths $E_z = 0.0$ (black solid line), 102.5 (red dashed line), 126.5 (blue dotted line), and 149.0 mV/a_z (dark cyan dash-dotted line) as a function of the electron energy. The length of the DSM quantum wire is taken as $L_x = 50a_x$. For clarity, the red dashed, blue dotted, and dark cyan dash-dotted lines are lifted entirely by 2.0, 4.0, and 6.0, respectively. (b) The same as (a) but as a function of the electric field strength. The electron energy $E = 72.0$ meV, as indicated by the vertical olive dotted line in (a).

and its strength is increased, as shown in Figs. 3(b)–3(d). Additionally, the symmetry of the transversally local charge density distributions along the z axis is broken and they are moved progressively toward the z-axis direction. This effect originates from that the electron is driven by the electric field force $\vec{f} = -eE_z\vec{z}_0$ (here $\vec{z}_0$ is a unit vector along the z axis), which affects the local charge density distributions along the z-axis direction. The local spin polarization density distributions $\rho^S = \sum_o [|\phi_{m,n,k_x}^{o,\uparrow}(y,z)|^2 - |\phi_{m,n,k_x}^{o,\downarrow}(y,z)|^2]$ corresponding to Figs. 3(a)–3(d) are shown in Figs. 3(e)–3(h), respectively. For the DSM quantum wire without electric field, the local spin polarization density is almost zero everywhere due to the overlap of the two different spin states, as shown in Fig. 3(e). However, for the DSM quantum wires with electric field, there are only oppositive spin-polarized charge densities near the two surfaces $y = 0$ and $y = 20a_y$ since the bulk charge densities are eliminated, as shown in Figs. 3(f)–3(h), demonstrating that the helical surface states present in the system. The evolution of the transversally local charge and spin polarization density distributions of the DSM quantum wire under the varied electric field may prove indirectly that the TPT happens in this system.

In order to comprehend the evolution of the orbital-resolved energy bands and electronic states with increasing electric field strength shown in Figs. 2 and 3 more clearly, we calculate the spin-resolved topological Chern number of the considered system. For simplicity we take a DSM thin film with z-axis confinement as an example to clarify the effect of the electric field on the spin-resolved topological Chern number since it is k_z dependent, as shown in Eq. (6). Figure 4(a) shows the first pair of energy subbands and band gap of the DSM thin film at $k_s = 0$ as a function of the electric field strength. The thickness of the thin film is chosen as the same as that of the quantum wire along the z-axis direction, i.e., $W_z = 6a_z$. The first conduction subband E_{C1} decreases monotonously while the first valence subband E_{V1} increases when the electric field strength is increased, as shown by the black and red solid lines in Fig. 4(a), respectively. Finally, they cross at $E_z^C = 67.6$ mV/a_z. As a result, the band gap of the DSM thin film is decreased gradually to be closed at the critical electric field strength. After that, the band gap is

reopened and its value is increased with increasing electric field strength, as shown by the blue dashed line in Fig. 4(a). Figure 4(b) demonstrates the spin-resolved topological Chern number of the first conduction subbands of the DSM thin film as a function of the electric field strength. According to Eq. (6), the spin-resolved topological Chern number of each subband of the DSM thin film without electric field is 0 so that it is a normal band insulator. However, for the DSM thin film with electric field, the spin-resolved topological Chern number of each conduction subband is computed by

$$C_{Cn}^{s_z} = \frac{s_z}{2}\left[\mathrm{sgn}(M_2) + \mathrm{sgn}\left(M_0 - M_1 k_{zn}^2 - \frac{|\Delta E_{Cn}| + |\Delta E_{Vn}|}{2} \right) \right], \quad (8)$$

in which ΔE_{Cn} and ΔE_{Vn} are the varied energy of the nth conduction and valence subbands at $k_s = 0$ after the electric field is applied. Therefore, the topological Chern numbers of both the first spin up and down conduction subbands keeps 0 until the band gap is closed, as shown by the dark cyan solid and magenta dashed lines, respectively. However, they transit to ± 1, which means that electrons with different spin states have oppositive group velocity, as the electric field strength is increased to $E_z^C = 67.6$ mV/a_z. The abrupt change of the spin-resolved topological Chern number indicates that normal-topological phase transition emerges at this critical electric field strength.

B. Electron transport in the two- and four-terminal DSM quantum wires

Figure 5(a) shows the total transmission probabilities spectra of the two-terminal DSM quantum wire with different electric field strengths as a function of the electron energy. The electric field strengths are the same as those in Figs. 2(a) and 2(c)–2(e), respectively. For clarity, the red dashed, blue dotted, and dark cyan dash-dotted lines are lifted wholly by 2, 4, and 6, respectively. Quantized steps with the values $2j$
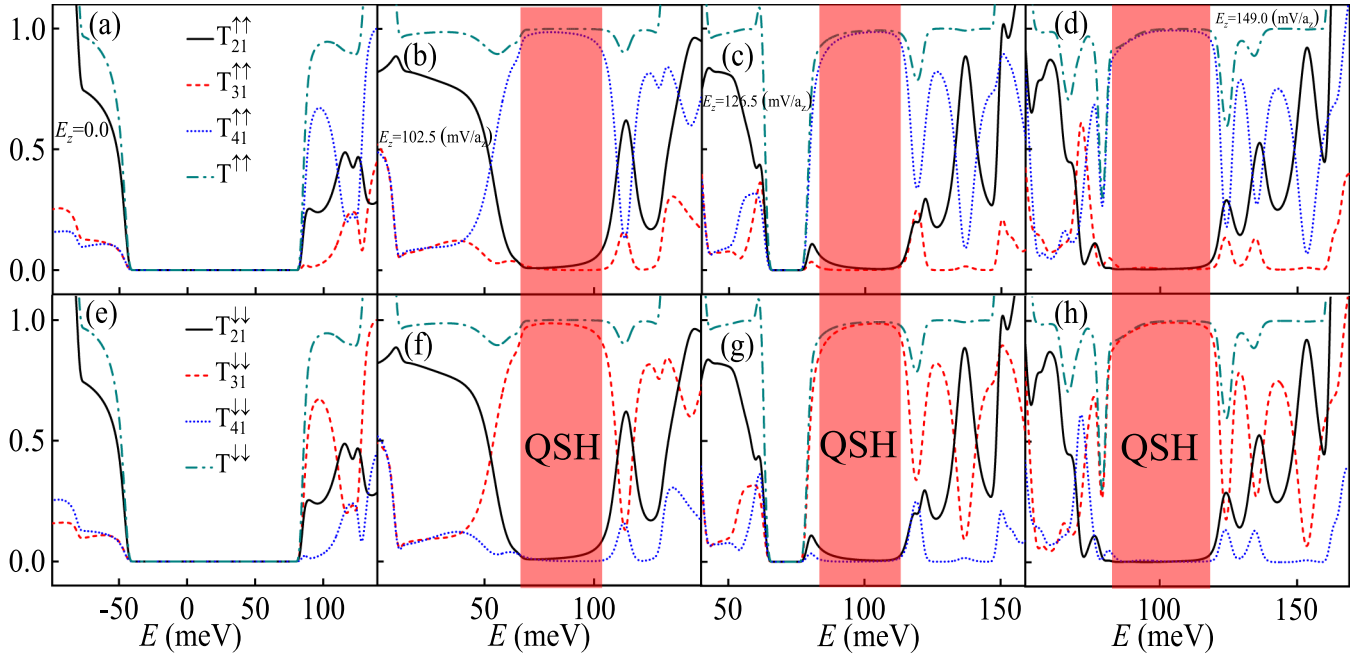
FIG. 6. The transmission probability spectra for the spin-up electrons in the four-terminal DSM quantum wire with different electric field strengths $E_z = 0.0$ (a), 102.5 (b), 126.5 (c), and 149.0 mV/a_z (d). (e)–(h) The same as (a)–(d) but for the spin-down electrons. The length of the DSM quantum wire is taken as $L_x = 20a_x$.

($j = 0, 1, 2, \ldots$) are obtained in the total transmission probability spectra. This transport behavior can be understood by the energy bands of the DSM quantum wires in Figs. 2(a) and 2(c)–2(e) since each occupied subband contributes a transmission quantum. It should be noted that no transmission gap is found for the case of $E_z = 102.5$ and 149.0 mV/a_z, as shown, respectively, by the red dashed and dark cyan dash-dotted lines; resulting from that the band gap of the DSM quantum wire is closed. For showing the electric field effects on the electron transport more clearly, Fig. 5(b) depicts the total transmission probability of the two-terminal DSM quantum wire as a function of the electric field strength. The electron energy $E = 72.0$ meV, as indicated by the vertical olive dotted line in Fig. 5(a). As the electron energy situates within the band gap of the DSM quantum wire first, the transmission probability keeps 0 until the strength of the electric field is increased to 81.0 mV/a_z. And then the lowest conduction subband of the DSM quantum wire is occupied so that the total transmission probability is transited to 2, i.e., the electron transport in the DSM quantum wire is switched on. As the electric field strength is increased further to 112.0 mV/a_z, the electron energy locates within the band gap again, leading to the switch-off of the electron transport. However, electron transport in the DSM quantum wire still can be turned on as the electric field strength is increased to 144.0 mV/a_z. The electron transport behaviors above indicating that it can be controlled by tuning the external electric field strength.

The transmission probability spectra of the four-terminal DSM quantum wire with different electric field strengths are shown in Fig. 6. As the electric field does not mix the two spin-dependent Hamiltonians $h_{\mathbf{k}}^{\uparrow}$ and $h_{\mathbf{k}}^{\downarrow}$ in Eq. (1) and there is no spin flipping mechanism in the investigated

system, the spin-dependent transmission probability between any two leads can be computed independently. The transmission probability spectra for the spin-up electron are shown in Figs. 6(a)–6(d) while those for the spin down electron are given in Figs. 6(e)–6(h). The electric field strengths are also the same as those in Figs. 2(a) and 2(c)–2(e), respectively. Due to the structural symmetry of the four-terminal DSM quantum wire, the longitudinal transmission probabilities for the spin-up and spin-down electron are the same, that is, $T_{21}^{\uparrow\uparrow} = T_{21}^{\downarrow\downarrow}$, as represented by the black solid lines. In addition, the four-terminal DSM quantum wire without/with an electric field also owns the time reversal symmetry so that the transversal transmission probabilities obey the rule $T_{31}^{\uparrow\uparrow}(T_{41}^{\uparrow\uparrow}) = T_{41}^{\downarrow\downarrow}(T_{31}^{\downarrow\downarrow})$, as shown by the red dashed and blue dotted lines. These transversal transport behaviors coincide well with the transversally local charge and spin density distributions demonstrated in Fig. 3. For the DSM quantum wire without electric field, the spin-dependent transmission probabilities vary with the increasing electron energy within the region where the lowest conduction band is occupied, as shown in Figs. 6(a) and 6(e). These results indicate that a variable spin Hall transmission probability $T^{\mathrm{SH}} = (T_{41}^{\uparrow\uparrow} - T_{31}^{\uparrow\uparrow}) + (T_{31}^{\downarrow\downarrow} - T_{41}^{\downarrow\downarrow})$, i.e., spin Hall effect can be observed in the considered system. However, for the DSM quantum wire with electric field, the transversal spin-dependent transmission probabilities are quantized ($T_{41}^{\uparrow\uparrow} = T_{31}^{\downarrow\downarrow} \approx 1$ and $T_{31}^{\uparrow\uparrow} = T_{41}^{\downarrow\downarrow} \approx 0$), as shown in the red regions in Figs. 6(b)–6(d) and 6(f)–6(h). More importantly, the longitudinal spin-dependent transmission probabilities $T_{21}^{\uparrow\uparrow}$ and $T_{21}^{\downarrow\downarrow}$ almost drop to 0. This transport effect agrees with the spin-resolved topological Chern number shown in Fig. 4(b). Therefore, quantum spin
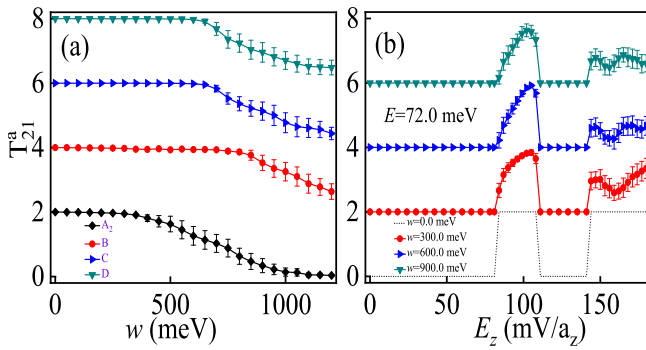
FIG. 7. (a) The ensemble average transmission probability spectra of the disordered DSM quantum wire as a function of the disorder strength. The electron energies are the same as those of the points A_2, B, C, and D in Figs. 2(a) and 2(c)–2(e), respectively. (b) The same as (a) but as a function of the electric field strength. Except for the disorder strength, other parameters are the same as those in Fig. 5(b). The error bars in (a) and (b) denote the transmission probability fluctuations and the number of the disordered DSM quantum wire samples is chosen as 200. For clarity, the red circle, blue right triangle, and dark cyan inverted triangle lines are lifted entirely by 2.0, 4.0, and 6.0, respectively.

Hall (QSH) effect can be achieved in these cases, indicating that the spin-momentum locked helical surface states in this system. The change of the transport behaviors of the four-terminal DSM quantum wire without and with external electric field proves further that the TPT happens in the system.

C. Disorder effects on the electron transport

The robustness of the electron transport against disorders is another important feature to distinguish the topologically trivial and nontrivial phases. Therefore, the disorder effects on the electron transport in the two-terminal DSM quantum wire with different electric field strengths are investigated in this subsection. The effects of the disorder-induced scattering on the total transmission probability can be modeled by applying a random fluctuation potential within the range $[-\frac{w}{2}, \frac{w}{2}]$ to the on-site energies of the discretized Hamiltonian in Eq. (1) [22,27]. Here the fluctuation amplitude w represents the disorder strength. In the following numerical calculations, the disorders are assumed to only exist in the DSM quantum wire (scattering region) and be distributed randomly in the whole wire (the disorder density is 100%), namely a stochastic potential is added to all the lattices of the discretized quantum wire.

Figure 7(a) shows the average total transmission probability $T_{21}^a = \langle T_{21} \rangle$ spectra of the disordered two-terminal DSM quantum wire with different electric field strengths as a function of the disorder strength. Here $\langle \cdots \rangle$ means averaging over an ensemble of samples with different realizations of disorder. Number of the disordered DSM quantum wire samples taken for the calculations is 200. The electron energies are taken as those for the points A_2, B, C, and D indicated in Figs. 2(a) and 2(c)–2(e), respectively. The error bar in each line represents the fluctuation of the two-terminal transmission probability $T_{21}^f = (\langle T_{21}^2 \rangle - \langle T_{21} \rangle^2)^{1/2}$. For the purpose of clearness, the

red circle, blue right triangle, and dark cyan inverted triangle lines are lifted wholly by 2, 4, and 6, respectively. For the DSM quantum wire without electric field, the average total transmission probability decreases as the electric field strength is increased, as shown by the black diamond line. Furthermore, the average total transmission probability arrives at 0 when the disorder strength is increased to about 1000.0 meV, namely electrons will be localized inside the disordered DSM quantum wire. However, for the DSM quantum wire with electric field, the average total transmission probability remains unchange first and then drops slowly with the increasing disorder strength, as shown by the red circle, blue right triangle, and dark cyan inverted triangle lines. More importantly, the average total transmission probability maintains a finite value even when the disorder strength is increased to 1200.0 meV, indicating that the transport in DSM quantum wire is robust against strong disorder in these cases. The different transport behaviors between the disordered DSM quantum wire without and with the electric field also verify that normal-topological phase transition is generated in the considered system. Figure 7(b) shows the average total transmission probability spectra of the two-terminal DSM quantum wire without ($w = 0.0$) and with weak ($w = 300.0$ meV), medium ($w = 600.0$ meV), and strong ($w = 900.0$ meV) disorders as a function of the electric field strength. The electron energy is the same as that in Fig. 5(b). The idea transmission probability plateaus within the electric field strength windows displayed by the black dotted line are destroyed as the disorder effects are taken into account, as show by the red circle, blue right triangle, and dark cyan inverted triangle lines. However, a relative large transmission probability still can survive even when a strong disorder is added, as shown by the dark cyan inverted triangle line, especially within the first electric field strength window. Moreover, the switch-off regions where $T_{21}^a = 0$ is not influenced by the disorder. Therefore, the switching effect controlled by the external electric field can also be achieved in the disordered DSM quantum wire. Note that the results above are obtained by varying the fluctuation potential amplitude while fixing the disorder density. However, similar results can also be achieved when the disorder density is varied while the fluctuation potential amplitude is fixed since these two parameters are equivalent in describing the disorder strength.

IV. CONCLUSIONS

In conclusion, we have investigated the orbital-resolved energy bands, electronic states, topological Chern number, transport properties, and disorder effects of DSM quantum wire without/with an external electric field. By the comparison of the features of the DSM quantum wire without and with electric field, TPT controlled by the electric field in the DSM is identified. Furthermore, it is also found that the electron transport in the DSM quantum wire can be turned on or off by varying the electric field strength and shows a strong robustness against disorder. Consequently, a topological field effect transistor may be designed based on the considered system.
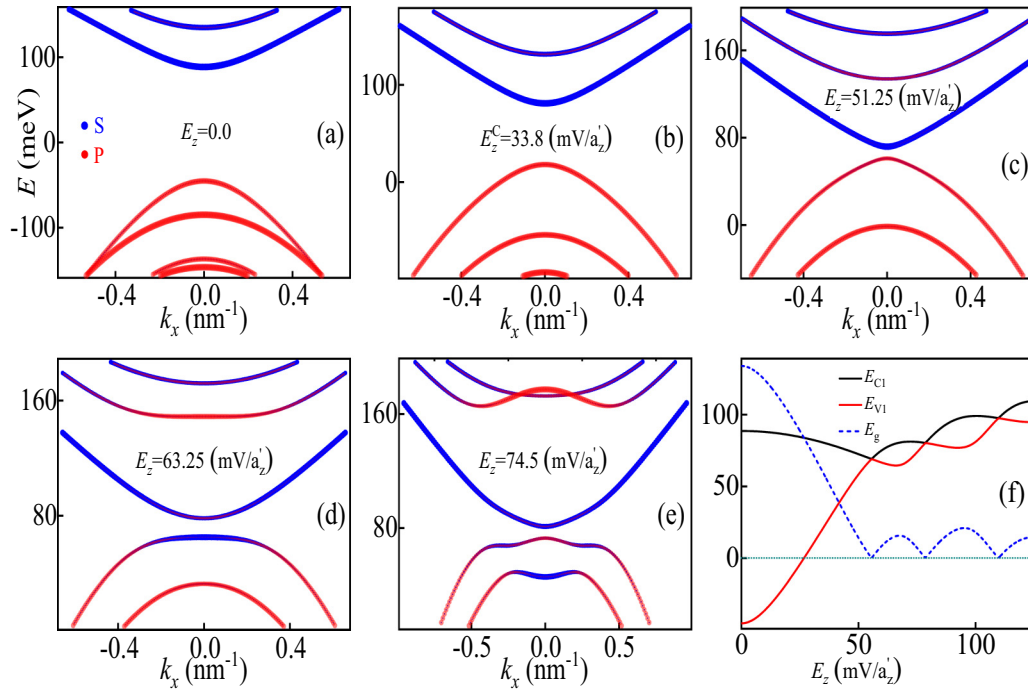
FIG. 8. The same as Fig. 2 but the lattice constants are set at $a'_x = a'_y = 0.2724$ nm and $a'_z = 0.2414$ nm.

APPENDIX: VALIDITY OF THE LATTICE HAMILTONIAN BASED ON THE FINITE-DIFFERENCE METHOD

The energy bands of the DSM quantum wire in Fig. 2, which are calculated from the discretized Hamiltonian of Eq. (1), is dependent on the choose of the number of nodes

or the lattice constants. For the same quantum wire, the larger number of nodes (smaller lattice constants) are taken, the more precise energy bands can be obtained. In order to show the validity of the numerical results obtained in the main text, we give another set of the orbit-decomposed energy bands of the DSM quantum wire in this Appendix, as shown in Fig. 8. All the parameters are the same as those in Fig. 2 but the lattice constants are taken as $a'_x = a'_y = 0.2724$ nm and $a'_z = 0.2414$ nm, which are a half of those in the main text, respectively. The results indicate that the energies of each subband in Fig. 2 are underestimated slightly (about 3–5 meV for the lower subbands). However, the intrinsic behaviors of the energy bands of the DSM quantum wire with increasing electric field strength are the same as those in Fig. 8. Therefore, the numeric results in the main text are reliable.

[1] M. Z. Hasan and C. L. Kane, Rev. Mod. Phys. **82**, 3045 (2010).

[2] X.-L. Qi and S.-C. Zhang, Rev. Mod. Phys. **83**, 1057 (2011).

[3] N. P. Armitage, E. J. Mele, and A. Vishwanath, Rev. Mod. Phys. **90**, 015001 (2018).

[4] C. L. Kane and E. J. Mele, Phys. Rev. Lett. **95**, 146802 (2005).

[5] B. A. Bernevig, T. L. Hughes, and S.-C. Zhang, Science **314**, 1757 (2006).

[6] S. M. Young, S. Zaheer, J. C. Y. Teo, C. L. Kane, E. J. Mele, and A. M. Rappe, Phys. Rev. Lett. **108**, 140405 (2012).

[7] Z. J. Wang, Y. Sun, X. Q. Chen, C. Franchini, G. Xu, H. M. Weng, X. Dai, and Z. Fang, Phys. Rev. B **85**, 195320 (2012).

[8] Z. J. Wang, H. M. Weng, Q. S. Wu, X. Dai, and Z. Fang, Phys. Rev. B **88**, 125427 (2013).

[9] M. König, S. Wiedmann, C. Brüne, A. Roth, H. Buhmann, L. W. Molenkamp, X. L. Qi, and S. C. Zhang, Science **318**, 766 (2007).

[10] H. M. Yi, Z. J. Wang, C. Y. Chen, Y. G. Shi, Y. Feng, A. J. Liang, Z. J. Xie, S. L. He, J. F. He, Y. Y. Peng, X. Liu, Y. Liu, L. Zhao, G. D. Liu, X. L. Dong, J. Zhang, M. Nakatake, M. Arita, K. Shimada, H. Namatame *et al.* Sci. Rep. **4**, 6106 (2014).

[11] S. Y. Xu, C. Liu, S. K. Kushwaha, R. Sankar, J. W. Krizan, I. Belopolski, M. Neupane, G. Bian, N. Alidoust, T. R. Chang, H. T. Jeng, C. Y. Huang, W. F. Tsai, H. Lin, P. P. Shibayev, F. C. Chou, R. J. Cava, and M. Z. Hasan, Science **347**, 294 (2015).

[12] V. Krueckl and K. Richter, Phys. Rev. Lett. **107**, 086803 (2011).

[13] F. Dolcini, Phys. Rev. B **83**, 165304 (2011).

[14] L. B. Zhang, F. Cheng, F. Zhai, and K. Chang, Phys. Rev. B **83**, 081402(R) (2011).

[15] X. Xiao, Y. Liu, Z. Liu, G. Ai, S. A. Yang, and G. Zhou, Appl. Phys. Lett. **108**, 032403 (2016).

[16] Y. Xu, Y. R. Chen, J. Wang, J. F. Liu, and Z. Ma, Phys. Rev. Lett. **123**, 206801 (2019).

[17] Y. Baba, Á. Díaz-Fernández, E. Díaz, F. Domínguez-Adame, and R. A. Molina, Phys. Rev. B **100**, 165105 (2019).

[18] X. B. Xiao, Z. F. Liu, Y. M. He, H. L. Li, G. P. Ai, and Y. Du, Chin. Phys. Lett. **32**, 127302 (2015).

[19] S. Tang, L. Zhou, Z. Liu, Q. Wu, Y. He, J. Luo, and X. Xiao, Phys. Rev. Appl. **14**, 054039 (2020).

[20] C. X. Liu, H. J. Zhang, B. Yan, X. L. Qi, T. Frauenheim, X. Dai, Z. Fang, and S. C. Zhang, Phys. Rev. B **81**, 041307(R) (2010).

[21] H. Z. Lu, W. Y. Shan, W. Yao, Q. Niu, and S. Q. Shen, Phys. Rev. B **81**, 115407 (2010).

[22] X. B. Xiao, S. A. Yang, Z. F. Liu, H. L. Li, and G. H. Zhou, Sci. Rep. **5**, 7898 (2015).

[23] R. Chen, D. H. Xu, and B. Zhou, Phys. Rev. B **95**, 245305 (2017).

[24] R. Chen, D. H. Xu, and B. Zhou, Phys. Rev. B **98**, 235159 (2018).

[25] K. Chang and W. K. Lou, Phys. Rev. Lett. **106**, 206802 (2011).

[26] M. S. Miao, Q. Yan, C. G. Van de Walle, W. K. Lou, L. L. Li, and K. Chang, Phys. Rev. Lett. **109**, 186803 (2012).

[27] H. Pan, M. Wu, Y. Liu, and S. A. Yang, Sci. Rep. **5**, 14639 (2015).

[28] B. Focassio, G. R. Schleder, A. Pezo, M. Costa, and A. Fazzio, Phys. Rev. B **102**, 045414 (2020).

[29] J. L. Collins, A. Tadich, W. Wu, L. C. Gomes, J. N. B. Rodrigues, C. Liu, J. Hellerstedt, H. Ryu, S. Tang, S. K. Mo, S. Adam, S. A. Yang, M. S. Fuhrer, and M. T. Edmonds, Nature (London) **564**, 390 (2018).

[30] Z. K. Liu, B. Zhou, Y. Zhang, Z. J. Wang, H. M. Weng, D. Prabhakaran, S.-K. Mo, Z. X. Shen, Z. Fang, X. Dai, Z. Hussain, and Y. L. Chen, Science **343**, 864 (2014).

[31] S. Datta, *Electronic Transport in Mesoscopic Systems* (Cambridge University Press, Cambridge, UK, 2003).

[32] T. Ando, Phys. Rev. B **44**, 8017 (1991).